Materials & Design 240 (2024) 112843

Contents lists available at ScienceDirect

Materials & Design

journal homepage: www.elsevier.com/locate/matdes

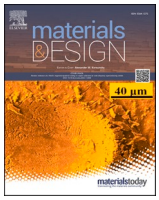

Damage-tolerant behavior of structural epoxies with thin PEI and PVDF interlayers

Dharun Vadugappatty Srinivasan, Anastasios P. Vassilopoulos *

Composite Construction Laboratory (CCLab), Ecole Polytechnique Fédérale de Lausanne (EPFL), Station 16, CH-1015 Lausanne, Switzerland

ARTICLE INFO

Keywords:
Composites
Fatigue
Fracture toughness
Damage tolerance
Thermoplastic
Crack arrest
Configurational material force

ABSTRACT

This work examines the crack-arresting capability of PEI and PVDF thermoplastic interlayers in short-glass fiber modified and core–shell rubber toughened epoxy materials under mode-I fracture loading. Experimental results show that the initial crack can be effectively arrested by the thermoplastic-epoxy interface and reinitiation of this crack at the thermoplastic layer requires up to 2.5 times higher load than the crack initiation load of the pristine epoxies. The interlayered designs also exhibit a significant increase in energy absorption by up to 43 times more than their pristine counterparts. Competing damage mechanisms and failure events are captured by microscopy images, digital image correlation and high-speed photography observations. Additionally, elasto-plastic fracture mechanics models based on configurational material forces theory are developed for a preliminary crack-arresting material selection and to elucidate the material inhomogeneity effects.

1. Introduction

High-performance polymeric materials are profoundly used in the manufacturing and assembly of lightweight structures. These materials are designed to meet specific strength, stiffness, and damage tolerance requirements. Although strength and toughness are difficult to attain simultaneously in engineered materials, many natural materials such as bones, nacre, glass sponges and dactyl clubs exhibit excellent strength and toughness [1–3]. These hierarchical biological materials are typically multi-scale composites, exhibiting a multitude of toughening mechanisms under damage, such as fiber debonding, fiber bridging, fiber pull-out, crack deflection, plastic energy dissipation, sliding, crack-tip blunting, and micro-cracking. These materials could achieve a maximum toughness of 2 to 6 times their initiation toughness [1]. By mimicking nature, a rare combination of strength and toughness can be devised for engineering applications as was shown, for example, with the brick and mortar, periodically arranged lamellar, spongy-porous, honeycomb and Voronoi tessellation designs [4,5]. In the aforementioned and other examples, material inhomogeneity is seen as the "universal" strategy for improving fracture toughness. Material inhomogeneity is achieved by a transition of different materials i.e., combining two or multiple materials and by forming distinct interfaces which can stop or delay the cracks originating from the free surfaces or inherent defects. Therefore, it is critical to design these multi-material structures with pertinent material inhomogeneity for damage-tolerance applications. For instance, based on the tensile modulus (E), yield strength (σ_y) and hardening coefficient/plasticity (n) of different materials, material inhomogeneity is classified as E-inhomogeneity, σ_y-inhomogeneity and n-inhomogeneity [6]. As per the Ramberg-Osgood type model, n refers to the hardening co-efficient of an elastic–plastic material. The implications of different material transitions on crack-tip shielding or anti-shielding can be explained with the following design cases:

- Case (a) - hard to soft transition: Can be realized by combining pristine (or parent) material with high E and/or σ_y with soft and compliant interlayer materials with low E and/or σ_y. Under the external loading, the crack driving force initially increases due to the lower strain energy density of the soft interlayer resulting in the crack-tip amplification (or anti-shielding). Due to this amplification, the crack approaches the low modulus and low strength interface quickly however, it is shielded within the interface and requires a high load for crack reinitiation.
- Case (b) - soft to hard transition: Can be obtained by combining pristine (or parent) material with low E and/or σ_y with hard and stiff interlayer materials with higher E and/or σ_y. Initially, crack-tip shielding occurs, as the hard interlayer has a high strain energy density and requires more load necessitating a low crack driving

* Corresponding author.
E-mail address: anastasios.vassilopoulos@epfl.ch (A.P. Vassilopoulos).

https://doi.org/10.1016/j.matdes.2024.112843
Received 6 June 2023; Received in revised form 19 December 2023; Accepted 9 March 2024
Available online 11 March 2024

force. Once the crack reaches the interface, the crack driving force is increased by the soft pristine material [7] resulting in crack-tip anti-shielding.

- Case (c) – weak hardening co-efficient (n) to strong n: Assuming both the parent and interlayer materials have similar E and σ_y but different n, the crack extension is impeded by the weaker plastic material due to the strong interaction between the crack-tip plastic zone and the interface [8]. The inverted design case assuming the transition of a material with strong n to a material with weak n is similar to case (a); the crack from the material with strong n approaches the interface with increased crack-tip driving force resulting in the crack-tip anti-shielding before arrested by the interface.

For a good crack-arresting interlayered design: (i) a large difference between the pristine and interlayer material properties and (ii) a combined E and σ_y-inhomogeneity over σ_y-inhomogeneity is recommended in [9]. As detailed in case (a), brittle materials with inherent micro-cracks are toughened by thin and multiple soft interlayers. Further, the fracture toughness is enhanced by increasing the interlayer thickness but not by only increasing the number of interlayers [7]. For example, a crack in a soda-lime glass plate (a brittle material) is effectively contained by a thick compliant epoxy adhesive layer than a thinner layer [10,11]. In contrast to this finding, another study reveals that the fracture toughness (K_{IC}) could not be increased by increasing the thickness of polyetherimide (PEI) interlayered soft epoxy material, although the thick interlayers improved the plastic work of fracture [12]. When the PEI layers are used with another stiffer epoxy material, a significant drop in K_{IC} occurred [12]. Soft polypropylene interlayers in talcum-reinforced polypropylene are used for crack-tip shielding but the interlayered specimens retain only 43 % to 72 % of the pristine polymer stiffness [13]. The reduction in stiffness is negated by increasing the tensile modulus and yield strength of the interlayer material but the crack-tip shielding could not be achieved in all scenarios. Due to the high tensile modulus, the interlayer is plastically deformed, leading to high crack driving forces [13]. From the perspective of the application, a carbon fiber reinforced polymeric (CFRP) composite layer is introduced in the wind turbine trailing edge joints, between the thick glass-fiber reinforced polymeric adherends and adhesive interface to arrest the transverse cracks originated due to residual stresses. PVDF interlayers are used in aerospace adhesive joints to arrest the crack or resist the fatigue crack growth for the required number of cycles [14,15]. In general, toughened epoxy materials are used to increase the damage-tolerance in these types of adhesive joints. Further, hybrid adhesives are developed to tailor the static and fatigue properties, but the resultant hybrid material properties are not higher than the pristine material properties [16–18]. Therefore, epoxy adhesive bond lines could be designed with interlayers to arrest and propagate the crack at a desired path. Besides these experimental investigations, finite element models are developed to explain the crack-tip shielding and anti-shielding phenomena based on several theories including small-scale yielding theory [8], near-tip and far-tip J integrals [19] and configurational material forces theory [20].

As shown in Fig. 1, most of the interlayer materials from the literature (blue circles) are more compliant ($E_{interlayer}/E_{pristine} < 1$) and weaker ($\sigma_{interlayer}/\sigma_{pristine} < 1$) than the pristine-homogeneous material (case a). The strength ratio is calculated with either yield or ultimate strength based on the literature data availability. The green point indicates the homogeneous, pristine material where both the modulus and strength ratios are equal to one. The main drawbacks of case (a) designs are (i) reduction in the stiffness due to compliant interlayers, (ii) crack-tip anti-shielding before crack arresting and (iii) questionable structural integrity of the compliant interlayers for the high-temperature applications. Another hypothesis is whether the highly toughened thermoplastics can be used as interlayer material (G-inhomogeneity) irrespective of their modulus and strength. To explore this hypothesis, the fracture behavior

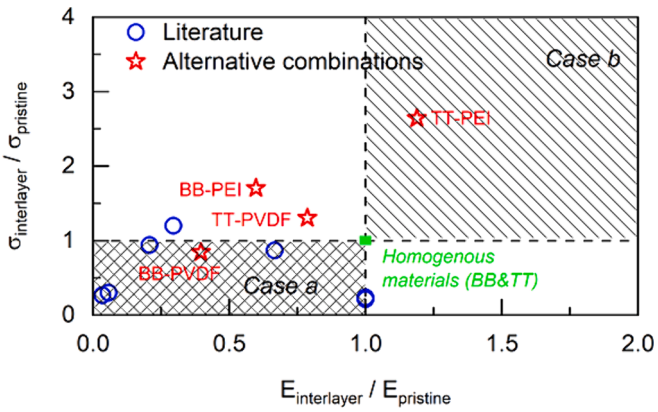

Fig. 1. Proposed pristine-interlayer material combinations.

of alternative combinations (red stars) must be investigated. Considering specimen geometry, single-edge-notch bending (SENB), compact tension, and single-edge-notch tension specimens are utilized to explore crack arresting, indicating this phenomenon is geometrically independent. While conventional methods like microscopic and SEM images are used in studying competing failure mechanisms, employing digital image correlation with high-speed photography is required for comprehensive understanding of full-field strain distributions and the dynamic fracture events.

In this work, polyvinylidene fluoride (PVDF) and polyetherimide (PEI) thermoplastic layers of 0.5 mm thickness are interlayered with short-glass fiber modified and core–shell rubber toughened epoxy materials. The constitutive properties of all materials are determined by uniaxial tensile experiments. Further, the damage tolerance of the interlayered materials is examined by single-edge-notch bending (SENB) specimens under mode-I fracture loading. The different failure mechanisms are documented using microscopy images, digital image correlation and high-speed photographs. Elasto-plastic fracture mechanics models based on configurational material forces theory are developed for evaluating the crack-tip shielding capability of PEI and PVDF materials under the ideal-interface assumption.

2. Materials and manufacturing

2.1. Epoxy and thermoplastic materials

Two different epoxy materials SPABOND™ (SP) 820HTA and SPABOND™ 840HTA provided by Gurit (UK) Ltd were used to fabricate the pristine and interlayered (IL) specimens. The two components of the as-received materials (epoxy base and hardener) include various fillers as schematically shown in Fig. 2a and 2b. Both epoxy materials have non-fibrous, sag-resistance fillers to maintain high-thickness bond lines in the wind turbine rotor blades. SP 820HTA is a non-toughened epoxy material (BB), primarily modified with short-glass fibers [21] whereas SP 840HTA epoxy material is a toughened epoxy material (TT) consisting of core–shell rubber particles [22].

Two unfilled amorphous thermoplastic materials, namely Ultem® 1000 PEI and Natural Kynar® PVDF were procured from Emco Industrial Plastics, Inc, USA for interlayering (0.5 mm thick) and for conducting uniaxial tensile experiments (3 mm thick). As these materials are widely used in structural applications and at high temperatures (>70 °C), they can be interlayered with a wide range of high-temperature curing epoxy materials without thermal degradation. Thin interlayers are judiciously selected as they are cost-effective and not expected to alter the stiffness when used with pristine epoxies.

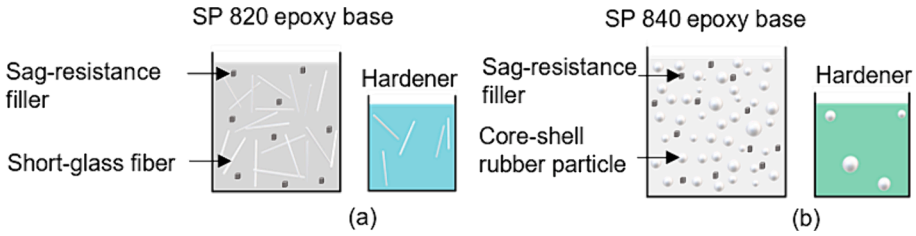

Fig. 2. Epoxy material systems: (a) SP 820HTA, non-toughened (BB) epoxy and (b) SP 840HTA, toughened (TT) epoxy.

2.2. Manufacturing of tensile and SENB specimens

For the tensile experiments, the non-toughened (BB) and toughened (TT) epoxy material panels with a nominal thickness of 4 mm were fabricated using the following steps. The epoxy base and hardener materials were manually mixed at a weight ratio of 100:34 using a wooden spatula. The hand-mixed material was degassed at 0.95 bar of vacuum for 7 min. The mixed epoxy was applied inside a release agent-coated aluminum mold of 4 mm thickness. The epoxy mixing, filling and additional dwell time at the ambient temperature of 20 ± 2 °C took 2 hrs. Following that the epoxy was cured inside a convection oven at 70 °C for another 2 hrs. The heating and cooling rate was maintained at 2 °C/min and 5 °C/min, respectively. The cured panels were water-jet cut according to ASTM D638-22 Type I specimen [23] whereas the Type I specimens of PEI and PVDF thermoplastics were cut from the as-purchased 3 mm thick plates.

For the fracture experiments, the pristine and IL epoxy SENB specimens (132 mm × 30 mm × 15 mm) were obtained from epoxy material blocks that were fabricated using aluminum molds following the same epoxy mixing and curing process as described above. The thermoplastic layers were placed at (A1) 1.5 mm from the initial notch tip. This position was arbitrarily selected to examine the crack-arresting capability of thermoplastic layers in the near-crack scenario. The aluminum mold consists of a bottom plate, and two 'E' (16.5 mm thick) and 'C' (13.5 mm thick) shaped bars to create a mold cavity of 30 mm. All mold parts were covered by a release agent (Sika® liquid wax- 815) before filling the epoxy. Considering the interlayering process, the thermoplastic layers of 0.5 mm thickness were sanded with 60 grit size paper using the Bosch sanding tool and then cleaned with water and acetone and conditioned at 40 °C for 10 min. For functionalizing the thermoplastic layer surfaces , 5 g of mixed epoxy was diluted with 20 ml of isopropanol and the epoxy primer solution was coated over the thermoplastic layers and dried at 35 ± 2 °C for 30 min.

The manufacturing steps of IL epoxies are shown in Fig. 3:

(a) Partial filling of epoxy (Fig. 3 – steps 1 + 2): The two 'E' shaped bars were fixed on the bottom plate to create a cavity in which the mixed epoxy material was manually filled using a scrapper.
(b) Interlayering (Fig. 3 – step 3): The functionalized interlayer was carefully placed on the epoxy and
(c) Complete filling of epoxy (Fig. 3 – step 4): The middle projection of 'E' bars was used to support the thermoplastic layers from sagging. The two 'C' shaped aluminum bars were fixed on the top of the 'E' bars and the mold cavity was filled with the remaining epoxy.

After placing the mold in an oven and curing for 2 h at 70 °C, the epoxy block was de-molded and four SENB specimens were obtained by abrasive water jet cutting. An initial notch (14.5 mm × 0.5 mm) was machined by a rotary saw and further sharpened with a sharp razor blade and abrasive paste. The initial crack length (a) of the prepared specimens was measured by an optical microscope, Dino-Lite AD7013MZT. It houses a 5-megapixel sensor that can magnify 240 times with a resolution of 2592 × 1944 pixels. The average initial crack length of non-toughened epoxy and toughened epoxy-based SENB specimens were 14.41 ± 0.8 mm and 15.27 ± 0.5 mm, respectively.

Table 1 shows the test matrix and design details of SENB specimen configurations based on the non-toughened (BB) and toughened epoxy-based materials (TT). The BB and TT materials are depicted as blue and green colors whereas the PEI and PVDF layers are shown in black and red colored lines, respectively. The alphanumeric 'A1′ in the specimen

Table 1
Test matrix and material details of the pristine and IL epoxy materials.

Specimen	Epoxy	IL material	Number of specimens	Schematic representation
BB	BB	–	4	
BBA1U	BB	PEI	4	
BBA1K	BB	PVDF	4	
TT	TT	–	2	
TTA1U	TT	PEI	4	
TTA1K	TT	PVDF	4	

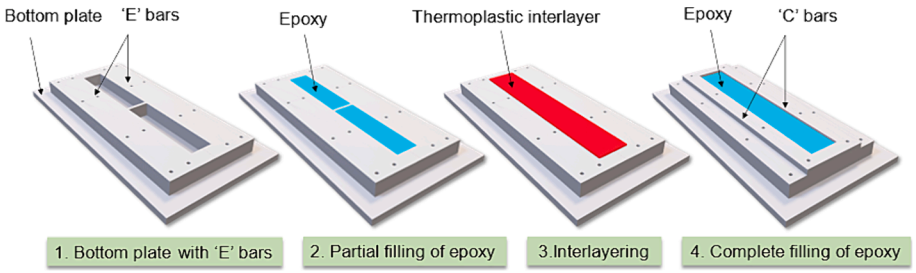

Fig. 3. Manufacturing steps of interlayered epoxy blocks.

names refer to the near crack position of interlayers whereas 'U' and 'K' denote the Ultem® 1000 PEI and Kynar® PVDF thermoplastic interlayer material, respectively.

3. Experimental and numerical methods

The uniaxial tensile experiments of pristine epoxies and thermoplastics for developing the elasto-plastic material models and single-edge-notch bending experiments for assessing the interlayering effect on fracture behavior were a part of the experimental investigation. Commercial finite element software, ABAQUS® from Dassault Systèmes [24] and Ansys® 2021R workbench from ANSYS Inc [25] were used to develop elasto-plastic fracture mechanics (EPFM) models based on the configurational material forces theory [26]. Fig. 4 shows the flow chart of the experimental and numerical methodologies employed in the current investigation. With the uniaxial tensile experimental results and fracture energy of pristine epoxies, the pristine and IL EPFM models were developed for selecting the interlayer material. Subsequently, SENB experiments of the IL specimens were conducted and their fracture performance was compared with the pristine material. Therefore, the fracture energy and load–displacement curves of BB and TT epoxy were briefly introduced in the FE modeling and results sections (Section 3.3 & 4.2).

3.1. Uniaxial tensile experiments

Uniaxial tensile experiments of epoxy and thermoplastic materials were performed using an MTS® 810 Landmark servo-hydraulic machine with a calibrated load cell capacity of 5 kN and applied load accuracy of ± 0.2 %. The ASTM D638-22 Type I tensile specimens were tested under displacement control, at a crosshead displacement rate of 1 mm/min. The 2D digital image correlation (DIC) technique was used to measure the engineering strain field on the specimens' surface. To consider the geometrical change of the specimen, only true stress ($\sigma_T = \sigma_E(1 + \epsilon_E)$) /strain ($\epsilon_T = ln(1 + \epsilon_E)$) values of the materials were presented instead of engineering stress (σ_E) /strain (ϵ_E) [27]. The strength was obtained from the peak force over the cross-sectional area of the specimens whereas the tensile toughness was calculated by integrating the area under the true stress–strain curve. Other parameters such as tensile modulus, failure strain and elastic and plastic Poisson's ratio were identified from the obtained true stress and strains. The constitutive properties of these materials were used in the finite element material models.

3.2. Single-edge-notch bending experiments

Single-edge-notch-bending experiments were performed using a walter + bai (w + b) test machine having a load cell capacity of 50 kN and applied compression load accuracy of 0.09 %, at an ambient temperature of 22 ± 3 °C and relative humidity of 40 ± 10 %. The specimen geometry, span-width ratio, initial notch-width ratio, roller diameter and loading rate (1 *mm/min*) were maintained as recommended by ASTM D5045-14 [28]. Fig. 5a shows the three-point bending fixture that consists of three steel rollers (left, right and top) having a diameter of 20 mm where the left and right roller supports were fixed at a span of 120 mm. The specimens were placed in the fixture and adjusted such that the initial notch and the contact point of the top roller were on the same loading axis. DIC images (2D) were captured during the experiments, at a frequency of 0.5 Hz for obtaining the specimen surface strain field. Two to four specimens were experimented with each design depending on the standard deviation of the results. High-speed photographs were

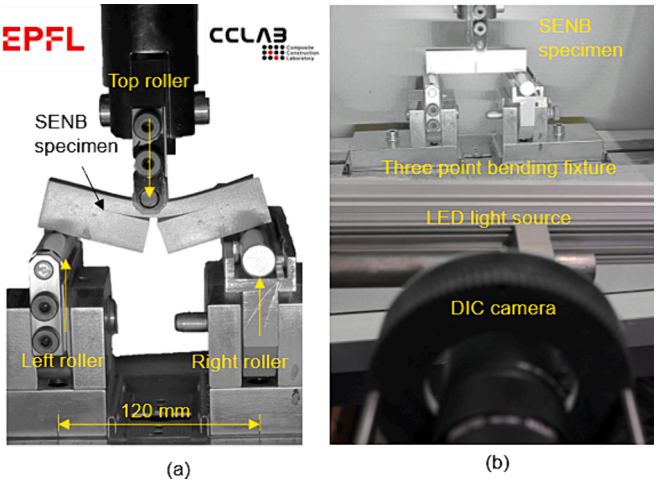

Fig. 5. Single-edge-notch bending experiment: (a) three-point bending fixture and (b) 2D-DIC setup.

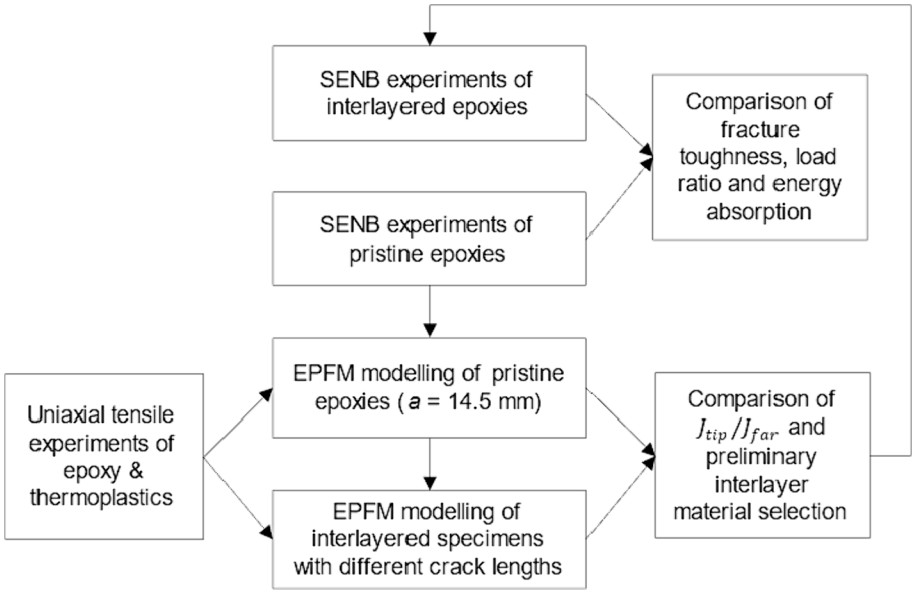

Fig. 4. Experimental and numerical methodology.

captured by FASTCAM SA-Z camera Photron® housing AF-S NIKKOR 50 mm lens. The imaging frequency was set to 60,000 frames per second to record the failure events.

3.3. Finite element modeling

Two-dimensional SENB models of pristine and IL specimens with dimensions of 130 mm × 30 mm × 15 mm with different initial crack lengths (Table 2, Fig. 6a and 6b) were developed meshed with a crack seam using Abaqus® 2019. The roller diameter and the interlayer thickness were 20 mm and 0.5 mm, respectively. Although Abaqus® 2019 software was particularly useful for meshing and inserting the initial crack seam, it does not comprise an in-built module for computing the configurational forces from the required contours. Hence, the meshed models were imported to Ansys® 2021R workbench software for analysis and post-processing and the configurational force values were easily obtained from an in-built fracture mechanics tool "material forces" [26]. Unlike conventional J-integral, configurational material forces theory can be used for any material model and the calculated crack driving force (J-integral) is contour dependent i.e., the J-integral at the near-tip (J_{tip}) and the far field (J_{far}) contours are different. The difference arises due to the material inhomogeneity term (C_{inh}) that is described as,

$$J_{tip} = J_{far} + C_{inh} \quad (1)$$

when crack shielding occurs, the effective crack driving force at the crack-tip reduces and the J_{tip} is smaller than the J_{far}, and therefore the C_{inh} is negative. In contrast to that, when the anti-shielding occurs C_{inh} becomes positive since J_{tip} is larger than J_{far}. In this modeling, an ideal interface is considered: (i) no defect at the interface, (ii) no interface debonding between the thermoplastic layer and epoxy material and (iii) once, the crack reached the interface, the reinitiation occurs at the epoxy without thermoplastic failure. With these modelling assumptions, the preliminary interlayer material selection can be carried out easily as the model requires only the tensile modulus of all materials and fracture energy of the pristine epoxies [29]. A total of 18 different models were created and listed in Table 2. The initial crack length was were increased from 14.5 mm to different positions in these 'A1′ (Fig. 6a), so the crack driving force ratio (J_{tip}/J_{far}) as a function of crack length can be derived . J_{tip}/J_{far} ratios ahead and beyond the interlayer interface were important to assess the crack-shielding or anti-shielding effect hence other crack-tip positions were not considered. Here, J_{tip} corresponds to the third contour from the crack-tip and J_{far} contour lies near the boundary as shown in Fig. 6c.

The elastic–plastic properties of epoxy and thermoplastic materials from the uniaxial tensile experiments were used as input for the linear-elastic and multi-linear isotropic hardening material models and no failure initiation or propagation criteria were implemented. The whole model meshed with 38,000 (pristine and 'A1′ models) 2D plane strain elements with reduced integration (CPE4R) elements. As shown in Fig. 6b, the SENB model fine meshed near the crack-tip, interlayer and roller contact regions. For instance, the crack-tip region of 10 mm × 6 mm (see close-view of Fig. 6b) meshed with 0.1 mm × 0.1 mm elements.

Table 2
List of the finite element models.

Model description	Model	Crack-tip positions in mm	Number of models
Pristine model of non-toughened epoxy	BB	14.5	1
Pristine model of toughened epoxy	TT	14.5	1
Near-positioned (A1), IL models of BB and TT-based epoxy.	BBA1U	14.5, 15, 15.5 and 17	4
	BBA1K		4
	TTA1U		4
	TTA1K		4

The bottom rollers were applied with simply supported boundary conditions i.e., only the rotation degree of freedom was allowed whereas the top roller was allowed to rotate as well as move along the y-axis. A single node from the top roller was selected as a master node whereas the other nodes were attributed as slave nodes and their degrees of freedom were constrained with an equation for applying vertical displacement and determining the corresponding reactive force along the y-axis. These values were used to plot the load and displacement response curves so the stiffness of IL specimens can be examined. Frictional contact (friction coefficient = 0.3) was used between the SENB specimen and the roller-contact region.

Initially, the pristine epoxy SENB models having an initial crack length of 14.5 mm (BB and TT) were subjected to a vertical displacement of 0.53 mm and 0.68 mm, respectively, to reach *J*-integral values of the far-field contour (J_{far}) of BB and TT models equivalent to the experimentally measured values of 1.57 N/mm and 1.36 N/mm. These J_{far} values were maintained in all 32 different IL models by adjusting the top roller displacement and their corresponding near-tip (J_{tip}) values were calculated to assess the inhomogeneity effect (refer Eqn.1).

4. Results and discussion

4.1. Uniaxial tensile behavior of epoxy and thermoplastic materials

The true stress versus true strain response of the epoxy materials and their DIC strain distribution before the final failure is shown in Fig. 7a. As the tensile strain increased, the stress was also increased linearly in BB and TT epoxy materials. Further increase in strain resulted in non-linear behavior with yielding in both materials and significant plastic deformation only in TT epoxy. This transition is described by 0.2 % offset yield strengths (σ_y) in BB and TT epoxy materials that are 61.5 ± 1.7 MPa and 37.9 ± 0.5 MPa, respectively. After the elastic limit, the microcracks and short-glass fiber debonding developed inside BB epoxy resulting in a gradual decrease in the tensile modulus. As can be seen in the DIC images of Fig. 7a, the high strain accumulated near the BB epoxy specimen edges from which a crack appeared and led to a sudden brittle failure. In the toughened TT epoxy, several micro-voids and their coalescence were created by the core–shell rubber particles, leading to higher plastic strain than the non-toughened epoxy (BB).

The true stress versus true strain response of PEI and PVDF thermoplastic materials is shown in Fig. 7b along with the 2D-DIC strain distribution at selected strain levels (indicated by the symbols on each curve). These curves shows that the initial elastic response of these amorphous polymers is primarily influenced by the van der waal forces, as exerted by the polymeric chains due to sliding phenomena. As the applied strain was increased, the yielding occurred, i.e., the localized stress inside the thermoplastics exceeded the van der waal forces resulting in constraints in the polymeric chain mobility [30]. The 0.2 % offset yield strengths (σ_y) of PEI and PVDF are 67.4 ± 3 MPa and 31.1 ± 1 MPa, respectively. Following the yielding process, the PEI polymeric chains permanently rearranged, necking happened due to high shear stress and subsequently the failure of the PEI occurred. As shown in the DIC images, the strain was localized near the failure region and the strain-softening was noticed in PEI after reaching the maximum stress of 117.4 ± 2.1 MPa. PVDF exhibited significant plasticity post-yielding and showed crazing from severe micro-void formation. The DIC images before the final failure show the opening and tearing of an edge crack that explains the sudden decrease in stress.

The strength versus modulus and tensile toughness versus true tensile failure strain plots of the materials are provided in Fig. 8a and 8b, showing that *E*-inhomogeneity, σ-inhomogeneity and their combinations could be achieved by selecting different epoxy-thermoplastic combinations. For instance, the combination of BB-PEI and TT-PVDF materials can be defined as a hard to soft transition in terms of *E*-inhomogeneity but a soft to hard transition in terms of σ-inhomogeneity

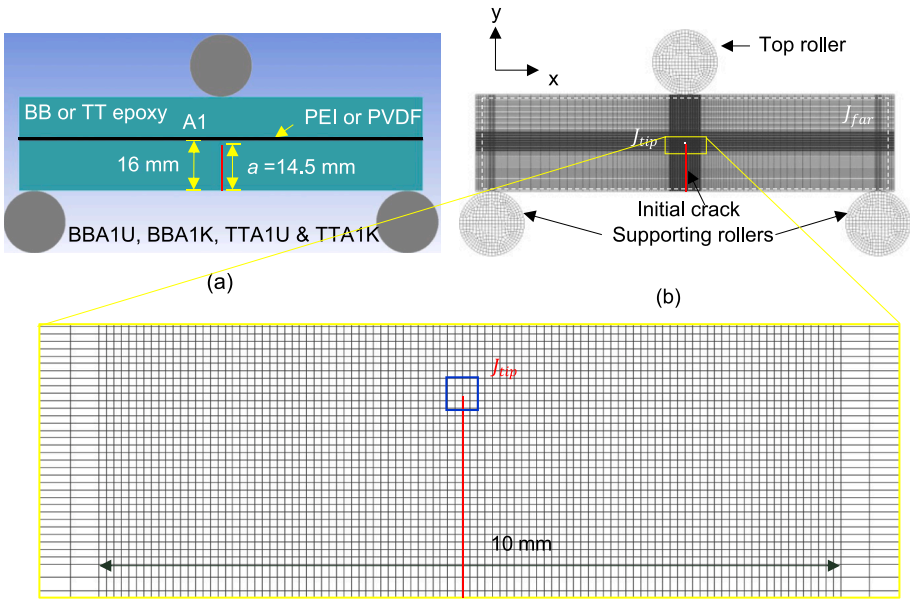

Fig. 6. FE modeling: (a) A1, near-positioned IL models and (b) typical meshing scheme of a full model with a close-view of the crack-tip meshing.

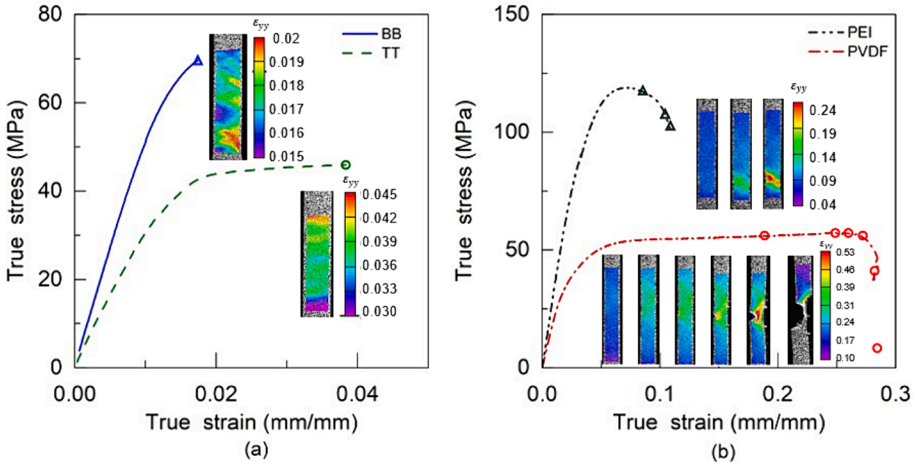

Fig. 7. True stress versus true strain response: (a) BB & TT epoxies and (b) PEI & PVDF thermoplastics.

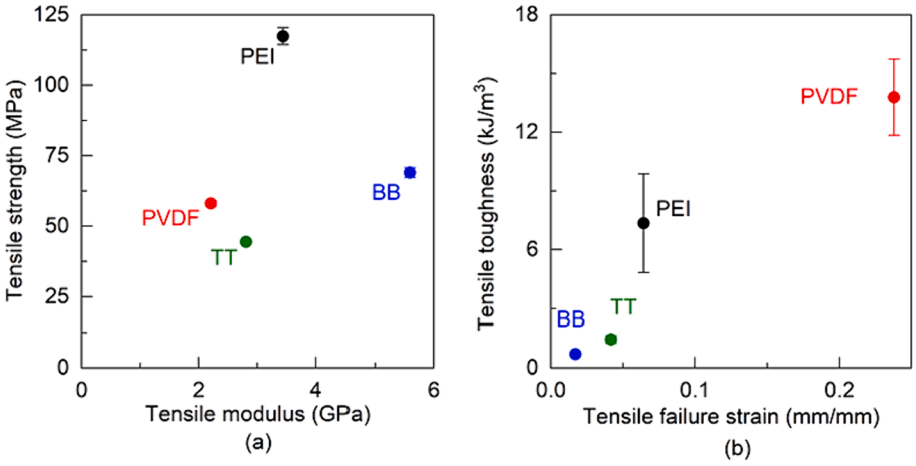

Fig. 8. Comparison of the tensile properties (a) modulus versus strength and (b) true tensile failure strain versus tensile toughness.

Table 3
Inhomogeneities of different epoxy and thermoplastic interlayer combinations.

Inhomogeneity	BB-PEI	BB-PVDF	TT-PEI	TT-PVDF
E- transition	Hard to soft	Hard to soft	Soft to hard	Hard to soft
σ- transition	Soft to hard	Hard to soft	Soft to hard	Soft to hard
G- transition	Soft to hard	Soft to hard	Soft to hard	Soft to hard

and *G*-inhomogeneity. Table 3 shows other possible material combinations and their inhomogeneities that can be achieved by using the examined materials. The selected thermoplastic layers are compliant or stiffer than the epoxy but always possess very high fracture energy. For instance, the fracture energy of PEI and PVDF is 3.17 N/mm [31] and 10 N/mm [32], respectively, at least 2 to 6.7 times higher than the considered epoxy materials (1.36 to 1.57 N/mm). The effect of these mismatching modulus, strength and toughness on the crack driving forces is assessed with the finite element modeling.

4.2. Finite element results based on configurational material forces theory

Fig. 9a shows the J_{tip}/J_{far} ratio of BB-PEI and BB-PVDF IL models for different crack length to width (a/W) ratios. As there was no inhomogeneity in the pristine material, the $J_{tip}/J_{far} = 1$ was indicated by dotted black line and used as the baseline value for comparison. Crack tip anti-shielding and shielding occurs when $J_{tip}/J_{far} > 1$ and $J_{tip}/J_{far} < 1$, respectively. When the a/W ratio is 0.483, the J_{tip}/J_{far} is only 1 % higher than the pristine material. When the crack-tip was positioned 0.5 mm ahead of the first BB epoxy-thermoplastic interface, the J_{tip}/J_{far} increases to a maximum of 3.3 % (BBA1U) and 5 % (BBA1K) as compared with the pristine material. It was due to a slight increase in the crack-driving force or anti-shielding. Despite that, PEI and PVDF thermoplastics are not expected to decrease the initial fracture toughness of the IL specimens significantly as compared with the pristine BB epoxy. Moreover, the crack could be effectively shielded by these two interlayers, as the $minJ_{tip}/J_{far}$ is 0.13, far lesser than one. Comparing PEI and PVDF interlayers, the former showed comparatively lesser anti-shielding and more shielding at non-toughened epoxy (BB) material. In the case of the TT epoxy-based IL models (Fig. 9b), only crack-tip shielding occurs ahead and beyond the IL. Under ideal-interface conditions, these designs are both damage-resistant and damage-tolerant. The fracture initiation toughness of these IL designs is expected to be slightly higher than the pristine TT epoxy material. Comparing PEI and PVDF interlayers, PEI shows a more crack-tip shielding effect ($minJ_{tip}/J_{far} = 0.088$) than PVDF ($minJ_{tip}/J_{far} = 0.105$) material.

The load and displacement response of BB and BB epoxy-based IL finite element models with an initial crack length of 14.5 mm are compared with the experimental result in Fig. 10a. The stiffness predicted by BB model (blue line) is 11.5 % higher than the experimental value (blue squares) and this difference can be attributed to the size effect. The tensile modulus measured from the ASTM D638-22 Type I specimen (3 mm × 4 mm) could be higher than the actual SENB specimen due to its larger dimension (30 mm × 15 mm), mainly influenced by the orientation of the short-glass fibers and the void distribution. Under ideal interface assumptions, the finite element model result shows that the initial elastic stiffness of the BB-based IL models was not affected by PEI or PVDF interlayers because of a low interlayer-pristine material volume percentage of 1.7 %. The load and displacement response of TT and TT epoxy-based IL finite element models ($a = 14.5$ mm) are compared with the experimental result in Fig. 10b and TT model has 15.5 % higher stiffness than the experimental value. The elastic stiffness of the TT epoxy and their IL models are similar, showing that PVDF and PEI thermoplastics can be used as interlayer materials without reducing the stiffness.

All the considered IL designs show crack-tip shielding beyond the interlayer irrespective of the interlayer modulus and strength. Further, the stiffness of the IL models was not reduced by thermoplastic interlayers. These models could be used for preliminary interlayer material selection, but they were developed based on the ideal interface assumptions without any failure criteria. Therefore, an experimental investigation of these designs should be carried out to assess their fracture and damage-tolerance performance using SENB specimens.

4.3. Fracture behavior of pristine and interlayered SENB specimens

The interlayered SENB specimens exhibit complex unstable fracture phenomenon (pop-ins) that limits the use of J-R curves as in thermoplastic materials [13]. Instead of J-R curves, the crack initiation and reinitiation loads, initial fracture toughness and area under the load–displacement curves (energy absorbed) of the pristine and IL epoxy materials are compared and discussed in the following sections and subsections.

4.3.1. Non-toughened epoxy (BB) based specimens

The load and displacement response of the short-glass fiber modified, non-toughened (BB) and PEI (BBA1U) and PVDF (BBA1K) interlayered epoxy specimens are compared in Fig. 11. The high-speed photographs during the failure event and final fracture surface images are shown in Fig. 12 and Fig. 13, respectively. The longitudinal strain (ε_{xx}) distributions of the specimens measured by the DIC at different peak load levels are compared in Fig. 14.

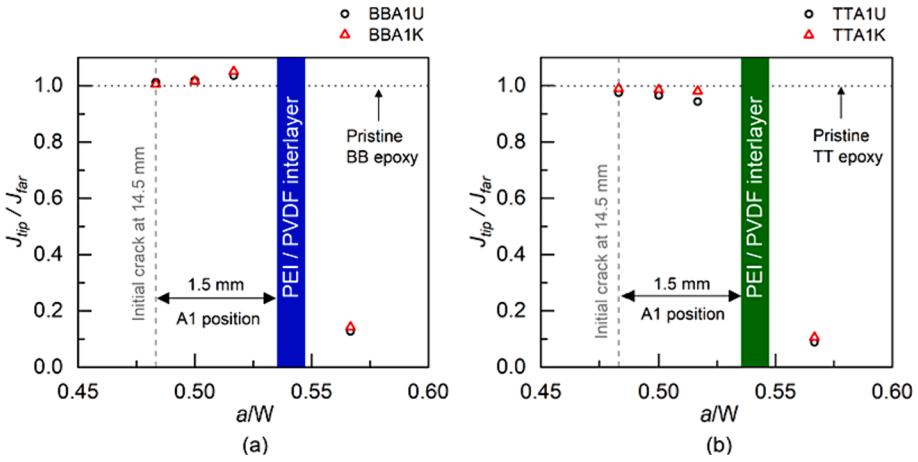

Fig. 9. The ratio of J-integrals at near-tip and far-field for different crack-tip locations: (a) near-positioned BB-based IL models and (b) far-positioned BB-based IL models.

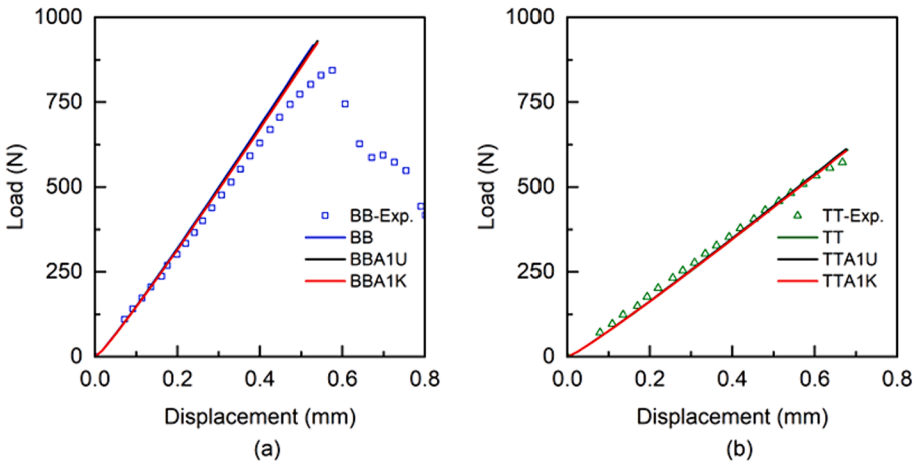

Fig. 10. Load versus displacement plots from the FE models: (a) BB-based SENB models and (b) TT-based SENB models.

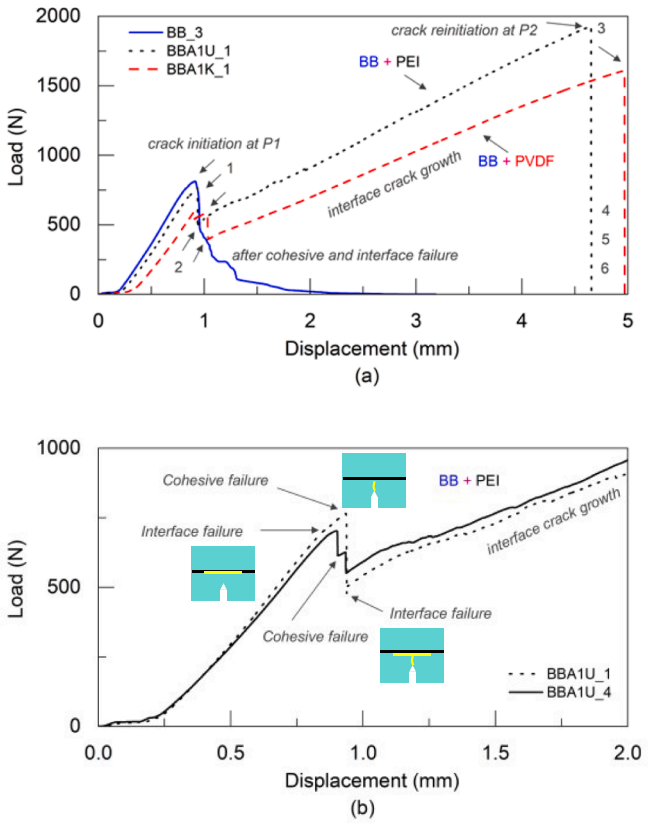

Fig. 11. Load versus displacement response: (a) BB_3 epoxy and the near-positioned IL, BB-based SENB specimens (BBA1U_1 & BBA1K_1) and (b) different failure modes of BB-PEI IL specimens.

All the specimens exhibited an initial non-linear region up to 30 N due to initial roller alignment, as discussed in ASTM D5045-14 [28]. As the displacement was increased further, BB epoxy material showed a linear increase in the load, reaching a maximum of 829 N. The ε_{xx} strain distribution at the crack initiation load (P1) is shown in Fig. 14, after which the load decreased moderately as the cohesive crack from the initial notch was propagated toward the loading point (refer blue curve in Fig. 11a). Eventually, a small crack resistance was provided by the short-glass fibers. The fracture surface of BB epoxy material shows different fracture mechanisms such as fiber breakage, fiber pull-out and fiber debonding (Fig. 13a). The macro-voids that resulted from the manual manufacturing process, noticed in the failure surface images (Fig. 13), are common in wind turbine adhesive joints [33].

In the PEI (BBA1U) interlayered specimens, a linear increase in the load was observed as the displacement increased. When reaching the initial peak load (P1) of 778 N, the specimens showed either an interface crack at the BB-PEI interface or a cohesive crack (in the BB material) from the initial notch (stage 1–2, Fig. 12). When the crack propagates in the pristine epoxy material and along the loading direction, it is defined as a cohesive crack whereas the interface crack is perpendicular to the loading direction and propagates along the epoxy-thermoplastic interface, also referred as interface debonding. For instance, Fig. 11b shows these two primary competing failure modes of PEI interlayered specimens. While the weakest area was the interface in BBA1U_4, the interface debonding occurred at first and the fracture ligament between the initial notch and the interface was intact. Following the interface debonding, the fracture ligament could not withstand more load, then a cohesive crack immediately originated from the initial notch and merged with the interface crack. This is a classic example of Cook–Gordan models of crack-stopping mechanisms, according to which the interface strength could be $< 1/5^{th}$of the cohesive strength of the pristine material [34].

In another specimen BBA1U_1, the interface was relatively strong and a cohesive crack initiated from the notch and suddenly reached the interface resulting in crack bifurcating and interface debonding. This phenomenon was very dynamic as the fracture ligament (the nominal distance between the initial crack-tip and PEI layer) is small, 1.5 mm. Notably, the initial peak load (P1) of these specimens was not significantly affected (<12 %) by these competing failure modes. The difference in failure modes can be attributed to the stress fields ahead of the crack-tip that are influenced by various parameters such as inherent defects ahead of the crack-tip and at the interface, the orientation of short-glass fibers, fracture ligament (length between the crack-tip and interlayer) and the initial notch quality. After the crack initiation, the load dropped suddenly to 511 N (stage 2, Fig. 11a). As the PEI layer has high fracture energy of 3.17 N/mm [31], the crack could not penetrate through it. The cohesive crack was completely arrested by PEI layer and propagated as an interface crack in a stick–slip manner as the displacement increased (stage 2–3, Fig. 11a). As shown in Fig. 12, the crack was formed like a 'T' shape, reached a certain crack length, and then stopped by the PEI layer. Due to this interface crack growth, the compliance of the specimen was increased, and importantly the load resistance was increased, a typical Cook–Gordan model of the crack-stopping mechanism. At a maximum failure load (P2) of 1966 N, the PEI layer failed and crack reinitiation occurred at BB epoxy material (stage 3 Fig. 11a and Fig. 12) due to the high bending-tensile stresses. The localized tensile strain (red color) at BBA1U in Fig. 14 indicates the

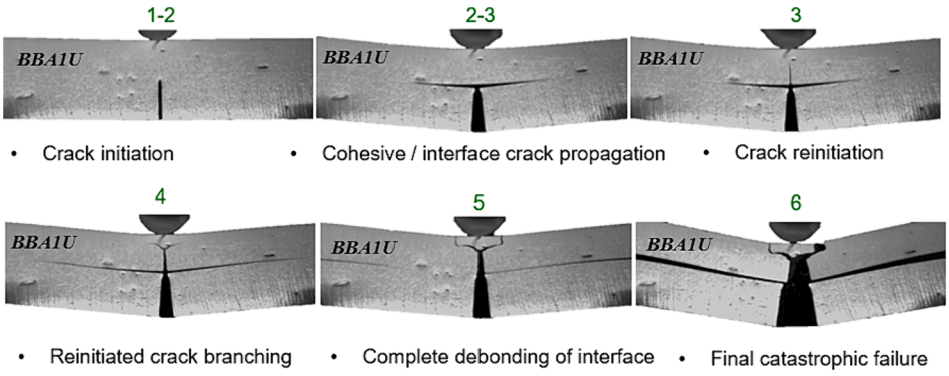

Fig. 12. High-speed photographs of the PEI interlayered (BBA1U) specimen during failure.

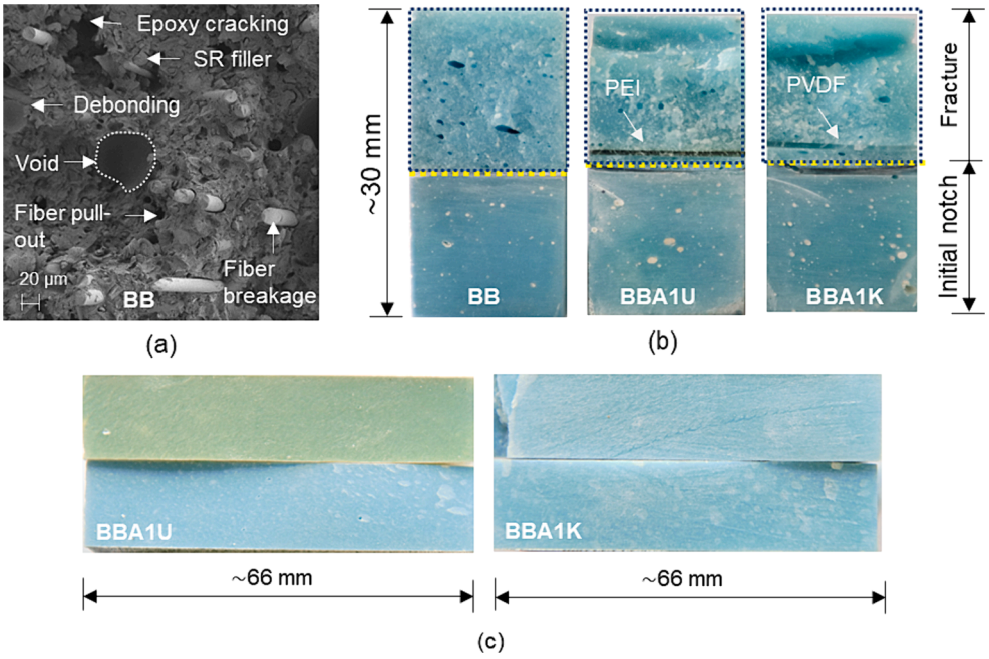

Fig. 13. Fracture surfaces: (a) SEM image of BB epoxy, (b) along the loading direction and (c) interface after complete debonding.

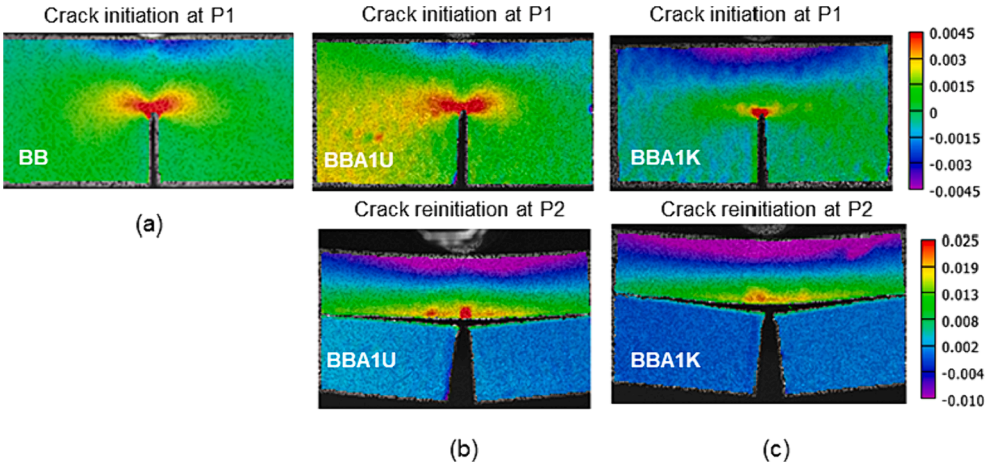

Fig. 14. ε_{xx} strain distribution during the crack initiation (P1) and reinitiation (P2) loads: (a) pristine non-toughened epoxy, BB, (b) BBA1U and (c) BBA1K.

crack reinitiation region. Stages 4 to 6 of the high-speed photography show the branching of reinitiated crack and complete debonding of the BB-PEI interface before the final catastrophic failure. The debonded interface failure surfaces are shown in Fig. 13c which indicates voids at the interface.

In the PVDF (BBA1K) IL specimens, the initial peak load (P1) was observed as 605 N. The failure process of BBA1K was like PEI (BBA1U) IL specimens whereas the final failure or crack reinitiation load (P2) was 1639 N. Fig. 11a shows that the initial stiffness of the IL materials is comparable with the pristine BB epoxy, as predicted by the numerical models. As seen in Fig. 14, the strain at the IL specimens (BBA1U and BBA1K) is more distributed at the P2 load and at least 5.5 times higher than at the crack initiation load (P1) of pristine epoxy (BB).

4.3.2. Toughened epoxy (TT) based specimens

The load and displacement response of the core–shell rubber particle toughened (TT), PEI (TTA1U) and PVDF (TTA1K) IL epoxy specimens are compared in Fig. 15. The high-speed photographs during the failure and the final fracture surface images are shown in Fig. 16 and Fig. 17, respectively. The 2D DIC strain (ε_{xx}) distribution of the specimens at different load levels is compared in Fig. 18. As the displacement was increased, TT epoxy material showed a linear increase in the load, reaching a peak value of 570 N. Then, a cohesive crack originating from the initial notch led to a sharp decrease in the load resistance. Although the failure was unstable and brittle in manner, the fracture surface exhibited a ductile-to-brittle transition region. A small ductile failure region near the initial crack was due to various fracture phenomena such as cavitation and tearing of core–shell rubber particles and crack pinning due to tail formations (refer Fig. 17a).

In the PVDF (TTA1K) IL specimens, a linear increase in the load was observed initially as the displacement was increased. The initial failure occurred at the TT-PVDF interface, prompting an initial non-linear behavior and a slight drop in the load resistance However, the ligament between the initial notch and interface was integral and withstood more load before failing at 383 N (stage 1–2, Fig. 15). This cohesive crack perpendicular to the PVDF interlayer was bifurcated (‘T’ shape) at the interface, causing another drop in the load. Here the crack was confined at the TT-PVDF interface and could not penetrate through the PVDF layer. In stage 2–3 (Fig. 15), the load resistance and compliance of the specimen were increased, as the crack propagated along the interface in a stick–slip nature (Fig. 17c). After a certain interface crack length, the crack growth was stopped by the PVDF layer (refer to small dashed-dot lines in Fig. 15) and by the plastic energy dissipation of TT epoxy. In this scenario, the interface crack driving force was reduced to zero and the applied load was stored and dissipated by both the interlayer and toughening particles. Because of this synergetic toughening effect, the tensile strain was high and relatively uniform over a region (refer Fig. 18b). As shown in stage 2–3, Fig. 16, the whitened area underneath the red dashed line and above the interface crack infers the coalescence of rubber toughening particles and micro-crack formations resulting from the plastic deformation of the material that could be cross-referenced with the DIC strain images. Due to the plastic energy dissipation, the load–deflection response was highly non-linear before the final fracture at (P2) 1341 N. The average crack reinitiation load of PVDF interlayered specimens is 2.35 times higher than the average crack initiation load of pristine TT epoxy material. Fig. 16 (stages 3–6) shows that several events occurred concurrently during the final failure: (stage 3) a crack appeared in the PEI layer and continued propagating perpendicular in the pristine material, (stage 4) the white line inside the yellow dashed oval shape 4 shows the acceleration of interface crack that led to complete debonding (stage 5) the primary crack was branched into two secondary cracks and (stage 6) finally, the specimen was shattered to dissipate the stored elastic strain energy inside the material. The residual curvature of the failed specimen confirms energy dissipation through plastic deformation and the final non-linear behaviour.

In the PEI (TTA1U) IL specimens, after reaching an initial peak load (P1) of 492 N, a sudden drop in the load (337 N) was noticed due to the TT-PEI interface failure. Following that, a cohesive crack originating immediately from the initial notch was merged with the interface crack (‘T’ shape). Here the crack was confined at the TT-PEI interface and could not penetrate through the PEI layer. Following that, the specimen was subjected to a higher load than P1 as the crack was propagated within the interface. The TT IL epoxy materials have shown the non-linear behavior before the final fracture at 1540 N.

Although, the numerical models showed no degradation in initial stiffness, the experimental results (Fig. 15) shows that IL materials have lower stiffness (19 % to 25 %) than the pristine material. The reduction in the stiffness could be due to the poor compatibility between the interlayer and TT epoxy. All the IL specimens exhibited a higher crack reinitiation load than the crack initiation load of pristine TT epoxy material. Fig. 18 shows the the strain in IL specimens (TTA1U and TTA1K) is distributed at P2 load and at least 14 times higher than at the crack initiation load (P1) of pristine toughened epoxy (TT).

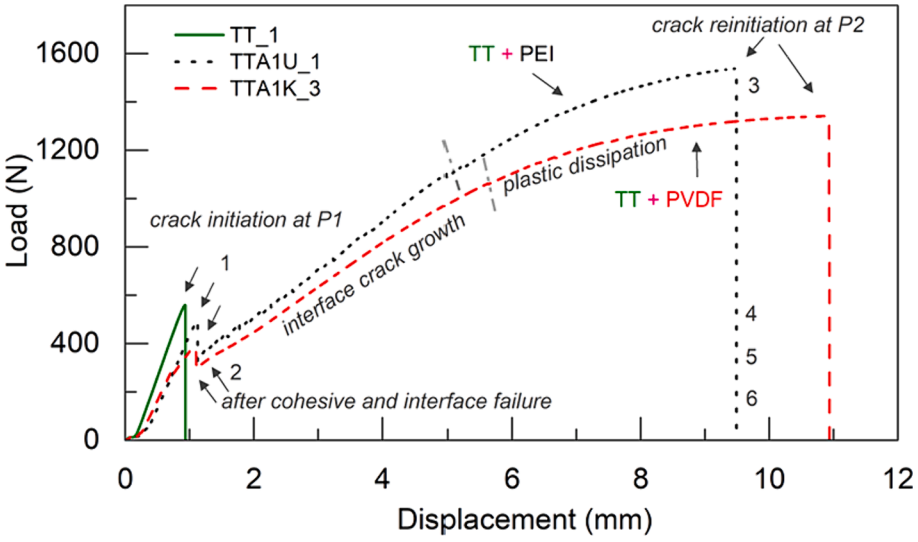

Fig. 15. Load versus displacement response of TT_1 epoxy and the near-positioned IL, TT-based SENB specimens (TTA1U_1 & TTA1K_3).

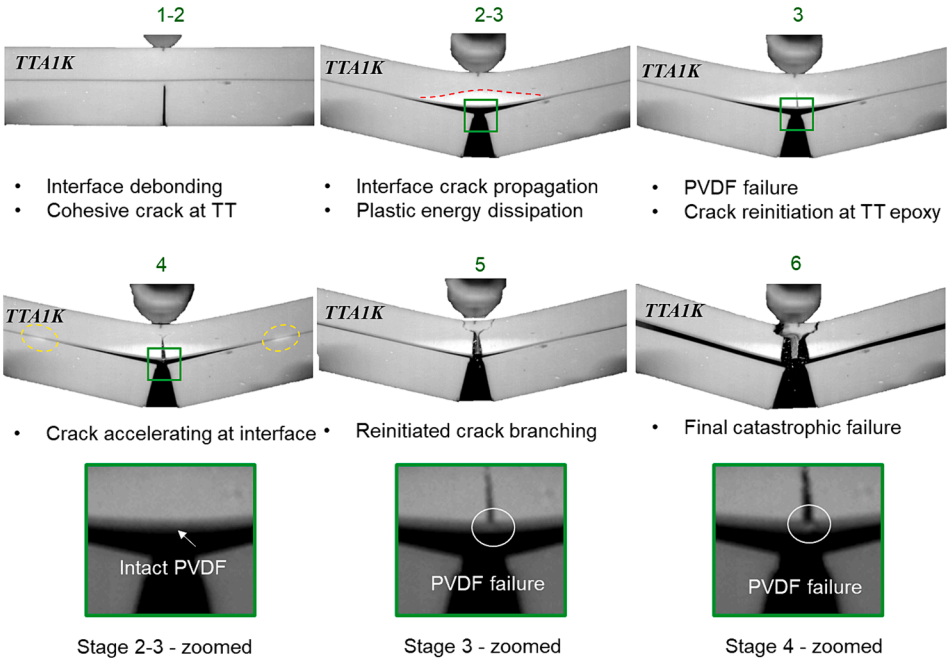

Fig. 16. High-speed photographs of the PEI interlayered (TTA1U) specimen during failure.

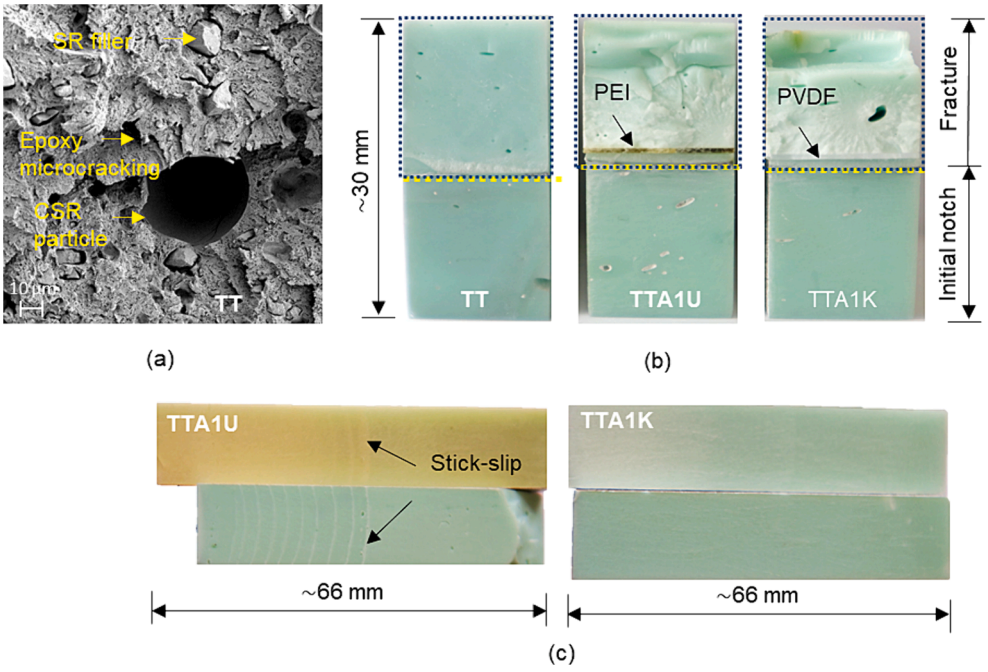

Fig. 17. Fracture surfaces: (a) SEM image of TT epoxy (b) along the loading direction and (c) interface after complete debonding.

5. Comparison of BB epoxy and their interlayered designs

The fracture performance of the pristine epoxy (BB) and IL designs (BBA1U and BBA1K) is assessed by comparing the initial fracture toughness, load ratio (P2/P1) and the normalized area under the load–displacement response ($U_{interlayered}/U_{pristine}$) as shown in Fig. 19a, 19b and 19c, respectively. The comparison of initial fracture toughness provides an overview of the crack-shielding or anti-shielding performance of IL specimens when the crack was ahead of the interlayer. The initial fracture toughness of the PEI interlayered epoxy (BBA1U) specimen was not affected by the PEI layer thanks to its better compatibility with the epoxy material. Although the tensile modulus of PEI was 62.5 % lower than that of BB epoxy, PEI has a high failure strength and strain to failure that prevented any increase in the crack-driving force (J_{tip}) ahead of the interlayer. Among the considered designs, the initial fracture toughness of the PVDF interlayered epoxy (BBA1K) specimen was only 0.78 times of the pristine epoxy (BB) due to the weak BB-PVDF interface energy. Overall, the experimented BB-based IL designs exhibited crack-shielding behavior beyond the interlayer, as predicted by FE models (Fig. 9a). The interface strength and toughness can be enhanced by optimizing the surface treatment process or altering the interlayer geometric features which are out-of-scope of this work. The curing cycle could not be modified to achieve interfacial dissolution and reaction-induced phase separation mechanisms for improving the interfacial

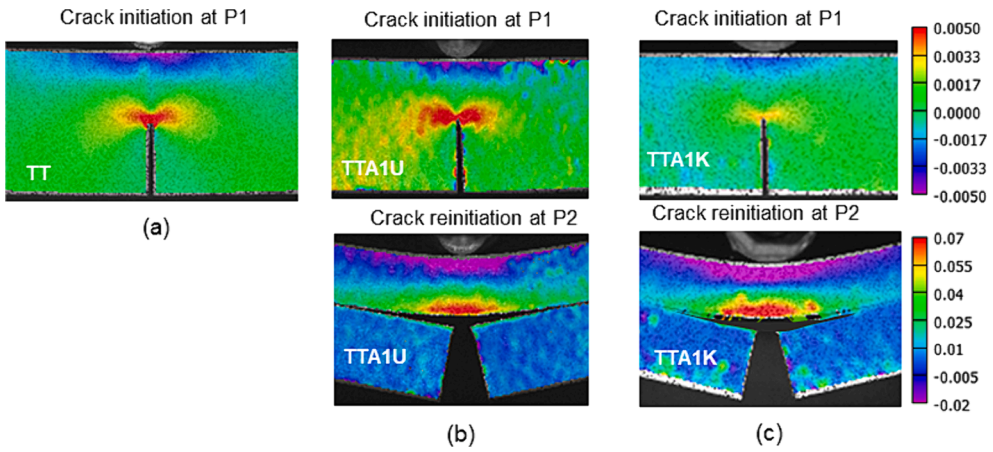

Fig. 18. ε_{xx} strain distribution during the crack initiation (P1) and reinitiation (P2) loads: (a) pristine toughened epoxy, TT, (b) TTA1U and (c) TTA1K.

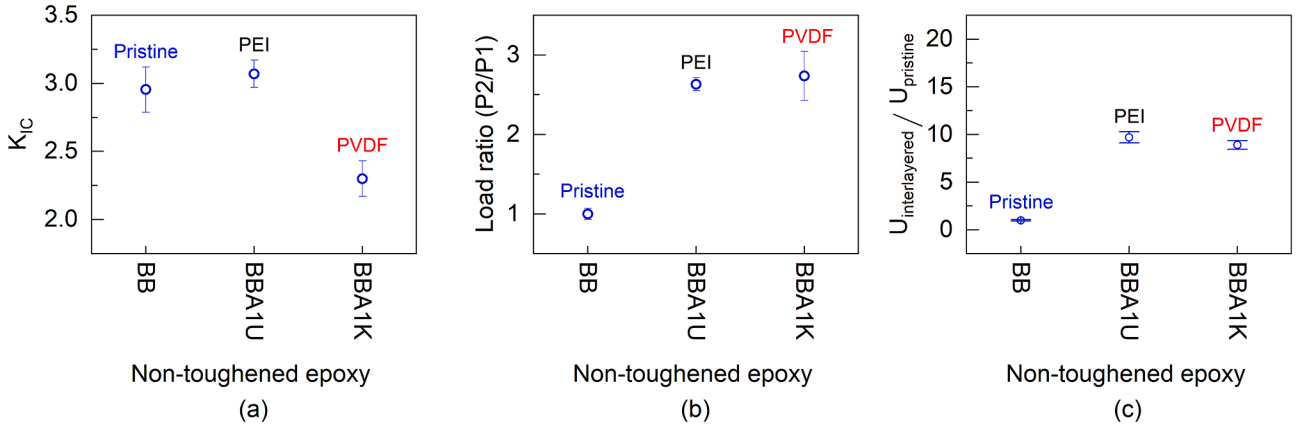

Fig. 19. Fracture characteristics of the non-toughened epoxy-based designs: (a) initial fracture toughness, (b) crack reinitiation to initiation load ratio and (c) energy normalized to the pristine material, BB.

bond strength [35]. Because these mechanisms occur at high temperatures (>160 °C), the wind turbine blade adhesive joints could not be processed at this elevated temperature range. When the interface toughness is improved, the drop in load after crack initiation may be reduced but the crack is still expected to propagate along the interface due to a significant mismatch in the fracture toughness of epoxy and thermoplastic interlayers.

6. Comparison of TT epoxy and their interlayered designs

The initial fracture toughness, load ratio (P2/P1) and the normalized area ($U_{interlayered}/U_{pristine}$) under the load–displacement response of TT-based designs are compared in Fig. 20a, 20b and 20c, respectively. The initial fracture toughness of TTA1U material was not affected by the PEI layer and there was no crack-tip shielding or anti-shielding. The

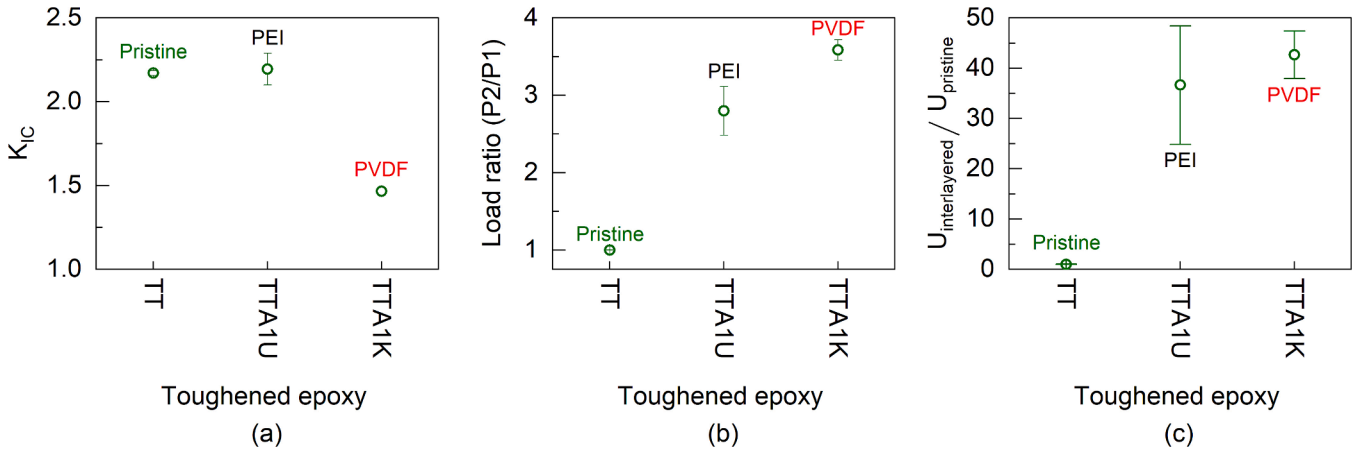

Fig. 20. Fracture characteristics of the toughened epoxy-based designs: (a) initial fracture toughness, (b) crack reinitiation to initiation load ratio and (c) energy normalized to the pristine material, TT.

tensile modulus and strength of PEI were 22.4 % and 164 % higher than TT epoxy, so this soft to hard transition prevented any increase in the crack-driving force. In contrast, the initial fracture toughness of TTA1K was decreased by 32.4 % as compared with TT material due to the poor compatibility between the epoxy and PVDF interlayer. The interlayered specimens exhibited multiple folds of increase in energy absorption up to 43 times as compared with pristine material because of the interlayering along with plastic energy dissipation and these increments pertain to SENB configurations. The increased standard deviation in the load and energy ratio of IL designs was due to the defects at the interface and in the epoxy material.

This study is focused on evaluating the quasi-static fracture performance of interlayered epoxy designs, revealing their considerable damage tolerance under such loadings. However, given that these structural epoxy materials are utilized in applications operating for extended periods and undergoing numerous fatigue cycles throughout their lifespan, it is imperative to investigate their performance under fatigue loading patterns as well. The fracture performance of interlayered materials can be influenced by factors such as thickness, position, and interface energy of the thermoplastic material. Exploring innovative approaches, such as incorporating perforated interlayers or employing 3D-printed architected layers, could be promising in arresting cracks and enhancing interface energy between the epoxy and the thermoplastic layers. Thick adhesive joints with crack arresting features could be realized in wind turbine rotor blades for enhancing their damage-tolerance and improving their structural integrity.

7. Conclusions

The crack arresting capability of non-toughened and toughened epoxy adhesives in the presence of PEI and PVDF interlayers was investigated in this work. FEM models based on the configurational material forces theory were developed to assist the preliminary interlayer material selection. The following conclusions were derived from the results:

1. Interlayered finite element models can be used to assess the stiffness of the interlayered material and crack shielding capability when the constitutive properties of the materials and the fracture toughness of pristine epoxy materials are known.
2. PVDF and PEI thermoplastic interlayers can effectively deflect and arrest the cracks emanating from near initiation sources in the non-toughened and toughened epoxy materials.
3. PEI showed better load resistance in both non-toughened and toughened epoxies due to its constitutive properties and better interface compatibility with the materials than PVDF.
4. Toughened epoxy-based designs showed enhanced toughening due to the synergetic toughening mechanisms of interlayering as well as plastic energy dissipation.
5. A reduction in load resistance due to the interface failure can be mitigated by enhancing the thermoplastic-epoxy interface energy. Although the weak interface energy reduced the initial fracture toughness, the final fracture toughness was improved by the interlayers significantly.
6. The main crack could be confined within the interface with well-toughened interlayers showing that, besides the tensile modulus, strength, and hardening component (n) that are usually suggested as the main crack-arresting material design parameters, the interlayer toughness should be also considered.

CRediT authorship contribution statement

Dharun Vadugappatty Srinivasan: Conceptualization, Data curation, Formal analysis, Investigation, Methodology, Writing – original draft. **Anastasios P. Vassilopoulos:** Conceptualization, Funding acquisition, Methodology, Supervision, Validation, Writing – review & editing.

Declaration of competing interest

The authors declare that they have no known competing financial interests or personal relationships that could have appeared to influence the work reported in this paper.

Acknowledgments

The authors wish to acknowledge the support and funding of this research by the Swiss National Science Foundation, Switzerland (https://www.snf.ch/en) under the project “Bonded composite primary structures in engineering applications (BONDS, Grant No. IZCOZ0_189905)”. The authors also acknowledge the experimental assistance provided by the technical team of the structural engineering experimental platform (GIS-ENAC at EPFL, Switzerland). The authors also thank Gurit for providing the adhesive materials. This article/publication is based upon work from COST Action CA18120 (CERT-BOND - https://certbond.eu/), supported by COST (European Cooperation in Science and Technology).

References

[1] J.W. Pro, F. Barthelat, The fracture mechanics of biological and bioinspired materials, MRS Bull. 44 (2019) 46–52, https://doi.org/10.1557/MRS.2018.324/FIGURES/3.
[2] R.O. Ritchie, The conflicts between strength and toughness, Nat. Mater. 10 (2011) 817, https://doi.org/10.1038/nmat3115.
[3] J.Q.I. Chua, D.V. Srinivasan, S. Idapalapati, A. Miserez, Fracture toughness of the stomatopod dactyl club is enhanced by plastic dissipation: a fracture micromechanics study, Acta Biomater. 126 (2021) 339–349, https://doi.org/10.1016/J.ACTBIO.2021.03.025.
[4] N.S. Ha, G. Lu, A review of recent research on bio-inspired structures and materials for energy absorption applications, Compos. B Eng. 181 (2020) 107496, https://doi.org/10.1016/J.COMPOSITESB.2019.107496.
[5] M. Mirkhalaf, T. Zhou, F. Barthelat, Simultaneous improvements of strength and toughness in topologically interlocked ceramics, PNAS 115 (2018) 9128–9133, https://doi.org/10.1073/pnas.1807272115.
[6] J.D. Pribe, T. Siegmund, J.J. Kruzic, The roles of yield strength mismatch, interface strength, and plastic strain gradients in fatigue crack growth across interfaces, Eng. Fract. Mech. 235 (2020) 107072, https://doi.org/10.1016/j.engfracmech.2020.107072.
[7] O. Kolednik, J. Predan, F.D. Fischer, P. Fratzl, Bioinspired design criteria for damage-resistant materials with periodically varying microstructure, Adv. Funct. Mater. 21 (2011) 3634–3641, https://doi.org/10.1002/adfm.201100443.
[8] S. Suresh, Y. Sugimura, E.K. Tschegg, The growth of a fatigue crack approaching a perpendicularly-oriented, bimaterial interface, Scripta Metallurgica Et Materiala 27 (1992) 1189–1194, https://doi.org/10.1016/0956-716X(92)90597-8.
[9] O. Kolednik, R. Kasberger, M. Sistaninia, J. Predan, M. Kegl, Development of damage-tolerant and fracture-resistant materials by utilizing the material inhomogeneity effect, J. Appl. Mech. Transactions ASME 86 (2019), https://doi.org/10.1115/1.4043829/726197.
[10] J.J.W. Lee, I.K. Lloyd, H. Chai, Y.G. Jung, B.R. Lawn, Arrest, deflection, penetration and reinitiation of cracks in brittle layers across adhesive interlayers, Acta Mater. 55 (2007) 5859–5866, https://doi.org/10.1016/j.actamat.2007.06.038.
[11] M. Mirkhalaf, A.K. Dastjerdi, F. Barthelat, Overcoming the brittleness of glass through bio-inspiration and micro-architecture, Nature Communications 2014 5 (1) (2014.1–9.) 5, https://doi.org/10.1038/ncomms4166.
[12] M. Grossman, D. Pivovarov, F. Bouville, C. Dransfeld, K. Masania, A.R. Studart, Hierarchical toughening of nacre-like composites, Adv. Funct. Mater. 29 (2019) 1806800, https://doi.org/10.1002/adfm.201806800.
[13] J. Wiener, F. Arbeiter, O. Kolednik, G. Pinter, Influence of layer architecture on fracture toughness and specimen stiffness in polymer multilayer composites, Mater. Des. 219 (2022) 110828, https://doi.org/10.1016/J.MATDES.2022.110828.
[14] M.J. Schollerer, J. Kosmann, D. Holzhüter, C. Bello-Larroche, C. Hühne, Surface toughening – an industrial approach to increase the robustness of pure adhesive joints with film adhesives, Proc Inst Mech Eng G J Aerosp Eng 234 (2020) 1980–1987, https://doi.org/10.1177/0954410020950071.
[15] T. Löbel, D. Holzhüter, M. Sinapius, C. Hühne, A hybrid bondline concept for bonded composite joints, Int. J. Adhes. Adhes. 68 (2016) 229–238, https://doi.org/10.1016/j.ijadhadh.2016.03.025.
[16] D.V. Srinivasan, A.P. Vassilopoulos, Manufacturing and toughening effects on the material properties of wind turbine blade adhesives, Polym. Test. 116 (2022) 107770, https://doi.org/10.1016/J.POLYMERTESTING.2022.107770.
[17] D.V. Srinivasan, A.P. Vassilopoulos, Fatigue performance of wind turbine rotor blade epoxy adhesives, Polym. Test. 121 (2023) 107975, https://doi.org/10.1016/J.POLYMERTESTING.2023.107975.

[18] D.V. Srinivasan, A.P. Vassilopoulos, Dataset for the hybrid non-toughened and toughened epoxy adhesive properties, Data Brief 47 (2023) 108912, https://doi.org/10.1016/J.DIB.2023.108912.
[19] A.S. Kim, S. Suresh, C.F. Shih, Plasticity effects on fracture normal to interfaces with homogeneous and graded compositions, Int. J. Solids Struct. 34 (1997) 3415–3432, https://doi.org/10.1016/S0020-7683(96)00225-9.
[20] O. Kolednik, R. Schöngrundner, F.D. Fischer, A new view on J-integrals in elastic-plastic materials, Int. J. Fract. 187 (2014) 77–107, https://doi.org/10.1007/s10704-013-9920-6.
[21] SPABOND^{TM} 820HTA fast curing structural epoxy adhesive. Full General Datasheet n.d.
[22] SPABOND^{TM} 840HTA fast curing structural epoxy adhesive. Full General Datasheet n.d.
[23] ASTM International. Standard test method for tensile properties of plastics. 2022. https://doi.org/10.1520/D0638-14.
[24] Dassault Systèmes. https://www.3ds.com/products-services/simulia/products/abaqus/abaqusstandard/.
[25] Ansys Inc. https://www.ansys.com/academic.
[26] Ansys Inc. Material Forces: A novel approach to fracture mechanics in ANSYS n.d. https://www.wildeanalysis.co.uk/wp-content/uploads/2016/07/Material-Forces-A-Novel-Approach-to-Fracture-Mechanics-in-ANSYS-White-Paper-PDF.pdf.
[27] M. Angelidi, A.P. Vassilopoulos, T. Keller, Displacement rate and structural effects on poisson ratio of a ductile structural adhesive in tension and compression, Int. J. Adhes. Adhes. 78 (2017) 13–22, https://doi.org/10.1016/J.IJADHADH.2017.06.008.
[28] ASTM International. Standard test methods for plane-strain fracture toughness and strain energy release rate of plastic materials. 2014. https://doi.org/10.1520/D5045-14.
[29] A. Tiwari, J. Wiener, F. Arbeiter, G. Pinter, O. Kolednik, Application of the material inhomogeneity effect for the improvement of fracture toughness of a brittle polymer, Eng. Fract. Mech. 224 (2020) 106776, https://doi.org/10.1016/j.engfracmech.2019.106776.
[30] Zuanetti B. Characterization of polyetherimide under static, dynamic, and multiple impact conditions. HIM 1990-2015 2013. https://stars.library.ucf.edu/honorstheses1990-2015/1548.
[31] K.Y. Kim, L. Ye, C. Yan, Fracture behavior of polyetherimide (PEI) and interlaminar fracture of CF/PEI laminates at elevated temperatures, Polym. Compos. 26 (2005) 20–28, https://doi.org/10.1002/PC.20062.
[32] L. Laiarinandrasana, M. Lafarge, G. Hochstetter, Accounting for porosity, time and temperature dependency in fracture mechanics concepts on polyvinylidene fluoride material, Eng. Fract. Mech. 76 (2009) 2766–2779, https://doi.org/10.1016/J.ENGFRACMECH.2009.06.003.
[33] Mishnaevsky L. Root causes and mechanisms of failure of wind turbine blades: overview. Materials 2022, Vol 15, Page 2959. https://doi.org/10.3390/MA15092959.
[34] J. Cook, J.E. Gordon, C.C. Evans, D.M. Marsh, A mechanism for the control of Crack propagation in all-brittle systems, Proc. R. Soc. Lond. A 282 (1964) 508–520.
[35] Q. Voleppe, W. Ballout, P. Van Velthem, C. Bailly, T. Pardoen, Enhanced fracture resistance of thermoset/thermoplastic interfaces through crack trapping in a morphology gradient, Polymer (guildf) 218 (2021) 123497, https://doi.org/10.1016/J.POLYMER.2021.123497.